Methodology for Obtaining Aerodynamic Coefficients for Unified Wind Loading Provisions in ASCE 7

Yitian Guo[1]; Jin Wang, M.ASCE[2]; Timothy John Acosta[3]; Stefano Brusco[4]; and Gregory A. Kopp, M.ASCE[5]

Abstract: The objective of this study was to develop a method to update and consolidate the aerodynamic coefficients that are currently in the directional procedure and envelope procedure for the Main Wind Force Resisting Systems (MWFRS) in Chapters 27 and 28 of ASCE 7-22. A large data set of wind tunnel data, including 85 building models with different geometries, was employed. Design pressure coefficients, and the zones on the building surfaces in which they apply, were developed to represent realistic spatial distribution patterns of the wind-induced pressures associated with critical structural responses. The pressure coefficient models, provided in a combined peak coefficient (GCp) form, are applicable to buildings of all (allowable) heights and aspect ratios. Nondimensional geometric parameters are used to capture the variations due to building shape and size for the pressure coefficients. The proposed provisions are a significant improvement in matching the wind tunnel data compared with existing provisions. **DOI: 10.1061/JSENDH.STENG-14983.**

Author keywords: Building aerodynamics; Main wind force resisting system; Building codes; Wind tunnel testing.

Introduction

In the ASCE 7-22 (ASCE 2022) provisions, two different approaches are provided to calculate wind loading on main wind force resisting systems (MWFRS). In the directional procedure of Chapter 27, a gust effect factor, G, is defined and used with mean area-averaged pressure coefficients, Cp. The peak design pressure coefficients are obtained by multiplying these two terms, $(G)(Cp)$. This analysis approach to the structural response for the winds of the atmospheric boundary layer was developed using Davenport's (1967) gust effect factor method. This method relies on the measurement technology of the time of its development, which primarily allows the measurement of mean load coefficients. The ASCE 7 coefficients were taken from wind tunnel tests by Akins et al. (1977). The gust effects were estimated based upon theoretical models that considered both the effects of the wind turbulence (called the background response, or buffeting) and structural dynamics (resonance). This method is permitted for structures of all heights. For flexible high-rise buildings, the structural dynamics tend to dominate the gust load effects. For low-rise buildings, which historically have been considered to be rigid, a single gust effect factor of $G = 0.85$ has been allowed for many versions of the standard. The entire gust effect model was updated by Solari (1993a, b), with the ASCE 7-98 (ASCE 2000) implementation, which was discussed in detail by Solari and Kareem (1998). However, the nearly 50-year-old aerodynamic coefficients have not been revisited even though the newer measurement technology of modern pressure scanners has enabled the possibility to examine the peak gust effects of the background response caused by turbulence.

The envelope procedure of the Chapter 28 provisions was developed for low-rise buildings based on the studies of Davenport (1977) and Stathopoulos (1979). The work was sponsored by the Metal Building Manufacturers Association (MBMA) and relied on newly developed pressure scanner technology. Davenport and Statholpoulos considered the range of reactions for low-rise metal frame buildings (e.g., moments within the frames), along with basic aerodynamic loads (e.g., uplift, base shear). Considering in particular the internal reactions, Davenport and Statholpoulos developed the envelope procedure whereby the pressure distributions produced the equivalent static loads without direct consideration of wind direction. Because low-rise buildings have been considered to be rigid, structural dynamics effects are neglected, and the background turbulent response governs. Using pressure scanner technology along with a pneumatic-averaging technique, Davenport (1977) and Stathopoulos (1979) utilized directly measured peak values, GCp. Chapter 28 has a single set of pressure coefficients, and basic building geometric parameters including the height, h, depth (longer plan dimension), d, and width (least plan dimension), w, are not considered. Although the building zones have some variations with building dimensions, the overall loads are roughly constant under this code model for all low-rise buildings, as shown by Wang and Kopp (2021a) and Kopp et al. (2025). However, low-rise buildings do have distinct aerodynamics that depend on the building shape, meaning that many low-rise buildings have loads that are distinctly different from those provided by Chapter 28. Additionally, the analysis by St. Pierre et al. (2005) indicated that the MWFRS loads on building components such as frames and bays

[1]Postdoctoral Associate, Faculty of Engineering, Western Univ., London, ON, Canada N6A 5B9. ORCID: https://orcid.org/0000-0003-2832-6507. Email: yguo287@uwo.ca

[2]Assistant Professor, Faculty of Engineering, Western Univ., London, ON, Canada N6A 5B9. Email: jwan2225@uwo.ca

[3]Doctoral Candidate, Faculty of Engineering, Western Univ., London, ON, Canada N6A 5B9. ORCID: https://orcid.org/0000-0002-5454-6063. Email: tacosta@uwo.ca

[4]Postdoctoral Associate, Faculty of Engineering, Western Univ., London, ON, Canada N6A 5B9. ORCID: https://orcid.org/0000-0003-0472-9133. Email: sbrusco@uwo.ca

[5]Professor, Faculty of Engineering, Western Univ., London, ON, Canada N6A 5B9 (corresponding author). ORCID: https://orcid.org/0000-0002-0784-3014. Email: gakopp@uwo.ca

Note. This manuscript was submitted on January 22, 2025; approved on June 2, 2025; published online on August 25, 2025. Discussion period open until January 25, 2026; separate discussions must be submitted for individual papers. This paper is part of the ***Journal of Structural Engineering***, © ASCE, ISSN 0733-9445.

may be significantly underestimated. As a result, the Chapter 28 provisions need to be re-examined as well.

Hence, it is worthwhile to consider how one may consolidate the provisions of Chapters 27 and 28 into a single unified method, while including results from state-of-the-art wind tunnel studies. The purpose of this study was to do just that—to consolidate the MWFRS provisions into a single method using modern data.

One of the primary issues in consolidating the methods for determining MWFRS wind loads is to develop improved methods that better account for the effects of building geometry on the aerodynamic loads. Wind pressures vary over the building surfaces both spatially and temporally. The ASCE 7 provisions capture these with the intent that, when the design pressures are applied to the building, the equivalent static loads enable the designer to capture the load effects acting on the structure. To achieve this requires that the pressure distributions in the load cases be representative of those acting on the building. Thus, to develop provisions requires examination of the loads acting on the range of distinct structure systems. However, because it is not possible to conceive of all possible scenarios, the results need to be sufficiently general that they are still accurate for structural systems or components not considered in the development of the provisions. In addition, the pressure distributions need to be simple enough to be implemented easily in the graphical or tabular format used in ASCE 7. The challenge is that the real pressure distribution patterns that create the peak structural responses can be complicated and can vary with different structural types, and these do not necessarily coincide with those associated with simple area-averaged wall or roof pressures (Ho et al. 1995). Thus, it is important to study these patterns and ensure that the load cases conform to them.

The objective of this study was to develop new aerodynamic coefficients and the building zones where they are applied, while addressing the above-mentioned limitations. The coefficients are provided in combined [GCp] form, applicable for buildings of all (allowable) heights and aspect ratios. The idea is that the load cases should (1) represent pressure distribution patterns that produce the peak structural responses based on the rigid building assumption; (2) be reasonably simple; and (3) effectively capture the geometric effects of the building shapes so that relatively few buildings have design loads that are significantly different from their true values.

Experimental Data Sources

To achieve the overall objectives, a large wind tunnel data set was needed. Three sets of wind tunnel data were employed in this study. The first two sets have been studied previously: (1) Western University's contribution to the National Institute of Standards and Technology (NIST) database for low-rise structures with low-slope and gable roofs; and (2) Western University pressure data for rectangular plan building models with flat roofs and plan ratios, d/w, varying from 1 to 4 and height ratios, h/w, varying from 1 to 8. Details of these two sets were presented by Ho et al. (2005) and Wang and Kopp (2021a, b), respectively. In addition, new wind tunnel tests were conducted in the boundary layer wind tunnel at Western University for buildings with 6:12 sloped gable and hip roofs and h/w varying from 0.2 to 2 and d/w from 1 to 2. Acosta et al. (2024) provided a detailed validation of these new data. Tables 1–3 provide the building geometries used herein. Details of the wind tunnel experiments are presented in the aforementioned references, and are not repeated for brevity.

Table 1. Test cases from NIST database for low-rise buildings with low-sloped and gable roofs in open terrain at a scale of 1:100

Building no.	Roof slope (tangent)	Width, w (m)	Depth, d (m)	Eave height, h_e (m)
1	1:12	24.38	38.1	12.19
2				9.75
3				7.32
4				4.88
5	0.25:12	24.38	38.1	12.19
6				9.75
7				7.32
8				5.49
9				3.66
10	1:12	12.19	19.05	12.19
11				7.32
12				5.49
13				3.66
14	1:12	48.77	76.2	12.19
15				7.32
16				5.49
17				3.66
18	1:12	36.58	57.15	12.19
19				7.32
20				5.49
21				4.88
22				3.66
23	0.5:12	15.24	30.48	4.88
24				3.66
25	0.5:12	15.24	53.34	4.88
26				3.66

Table 2. Test cases for mid and high-rise buildings with flat roofs in open terrain at a scale of 1:100

Building no.	Width, w (m)	Depth, d (m)	Roof height, h (m)
1	12	48	12
2		36	
3		30	
4		24	
5		18	
6		12	
7		48	24
8		36	
9		30	
10		24	
11		18	
12		12	
13	6	24	24
14		18	
15		15	
16		12	
17		9	
18		6	
19		24	48
20		18	
21		15	
22		12	
23		9	
24		6	

Table 3. Test cases for buildings with 6:12 sloped gable and hip roofs in open and suburban terrain at a scale of 1:100

Building no.	Roof Type	Width, w (m)	Depth, d (m)	Eave height, h_e (m)
1-6	Gable	24.38	24.38	4.88, 7.32, 9.75, 12.19, 24, 48[a]
7-12	Gable	24.38	38.1	4.88, 7.32, 9.75, 12.19, 24, 48
13-18	Gable	24.38	48	4.88, 7.32, 9.75, 12.19, 24, 48
19-23	Hip	24.38	24.38	4.88, 7.32, 9.75, 12.19, 24
24-29	Hip	24.38	38.1	4.88, 7.32, 9.75, 12.19, 24, 48
30-35	Hip	24.38	48	4.88, 7.32, 9.75, 12.19, 24, 48

[a]No suburban terrain.

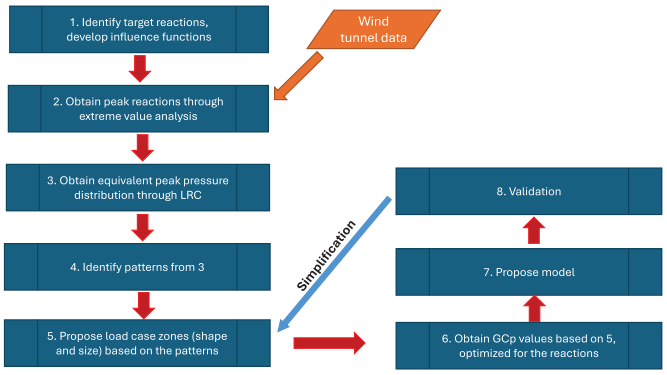

Fig. 1. (Color) Flowchart of the methodology for obtaining aerodynamic coefficients and load cases.

Determination of Peak Structural Loads and Responses for Rigid Buildings

The method for analyzing the data to develop the revised provisions is presented in Fig. 1. First, for each building model, the MWFRS responses of interest were identified and the peak values for these were obtained through analyses of the wind tunnel data. Typical patterns of pressure distribution that lead to these peak responses were determined via the load response correlation (LRC) method (Kasperski and Niemann 1992). These allow spatial zones with similar pressure coefficients to be identified and chosen. Following this, an optimization method was developed to obtain a best set of pressure coefficients considering all the different responses and buildings. Considering the resulting zone pressures and patterns, a design model with pressure coefficients and zones then was developed. The model was validated by comparing the model output with the experimental data, and then revised and simplified using a trial-and-error approach. The detailed methodology and results for each step are discussed in the next section. The remainder of this section discusses how the peak responses (Step 2) were obtained.

Target Responses and Influence Functions

For all buildings, the responses considered include overall uplift, torsion, and the base shear in two directions (and including base shear without the roof for the direction normal to the ridge). For low-rise buildings, additional responses were considered including bay uplift, bay thrust, and frame joint moments. This follows the conceptual approach of Stathopoulos (1979), who developed a series of influence functions for metal-frame, low-rise buildings. In particular, he assumed two-pin moment-resisting frames with 7.62-m (25-ft) bay spacing for moment-frame metal buildings. St. Pierre et al. (2005) and Wang and Kopp (2021a) used the same influence functions. Fig. 2(a) is a sketch of bay and frame spacing for a low-rise structure from the NIST database. Fig. 2(c) shows a schematic sketch of the two-pin moment-resisting frame. A linear influence function was applied to transfer the surface pressure to the frames [Fig. 2(b)]. The details of this approach were presented by Nywening (2006).

For mid- and high-rise buildings with flat roofs, the responses include the overall uplift, torsion, base shear, and base overturning moments in two directions, side wall loads, as well as floor-to-floor shear loads. The floor height was assumed to be 4 m (full scale). For all buildings, responses, terrains, and wind directions, time series of the responses were calculated from the wind tunnel pressure data.

Mechanical Admittance and Time Series Filtering

This work focuses on the background turbulent responses for rigid buildings; however, no building is truly rigid. To handle this, moving-average filters were applied to the time series in order to replicate the effects of the mechanical admittance to the turbulent gust (buffeting) loads. The averaging time of the moving-average filter was set to $1/3$ s (full scale) for buildings with $h/w \leq 2$ and $1s$ for $h/w \geq 4$. For h/w between 2 and 4, linear interpolation was applied. The filter length was determined by consensus of this project's advisory committee, considering assumptions of typical building parameters, because the mechanical admittance function is affected by both the natural frequency and damping ratio. Further details were presented by Guo et al. (2024).

The 3-s gust speeds were determined via a 3-s moving-average filter applied to time series of wind speed measurements in the wind tunnel. A shorter duration filter for the wind load implies that body-generated turbulence is playing a role in the background structural response. However, the theoretical gust response of the directional procedure (Chapter 27) explicitly neglects body-generated turbulence effects. In contrast, the development of the envelope procedure (Chapter 28) includes body-generated turbulence effects on rigid buildings because a rigid model was used and the only filtering included was based on instrumentation response and filtering required for data acquisition purposes. The effects of these assumptions were examined separately by Kopp et al. (2025).

Using the filter to capture mechanical admittance effects is both novel and philosophically different from filtering of pressure data from wind tunnel experiments in the past. Wind tunnel pressure data have long been filtered for tubing responses and the Nyquist criteria. Pressure data have been filtered to convert point pressures into equivalent area-averages using Lawson's (1980) method (see also Cook 1990; Holmes 1997), which can be considered as an equivalent aerodynamic admittance function (AAF). However, in the gust effect factor formulation of Solari (1993a, b) and Solari and Kareem (1998) the filter is not related to the AAF, which is accounted for separately. Solari and Kareem (1998) justified the use of a 3-s moving average filter as corresponding to the 3-s gust speed, which connects it explicitly to the quasi-steady theory. Kwon and Kareem (2014) argued that a 1-s moving average is the appropriate value. The current approach is consistent with that for mid- and high-rise buildings. The shorter duration filter for low-rise buildings ($1/3$ s) reflects the acknowledgment that building response, i.e., the mechanical admittance, plays a role in the loading for these buildings, even when they are considered rigid.

Peak Responses

The peak responses were assumed to follow a Gumbel distribution (Gumbel 1958; Cook and Mayne 1979). The parameters were obtained from the filtered response time series through the Lieblein BLUE approach (Lieblein 1974) using 16 segments. The Gumbel

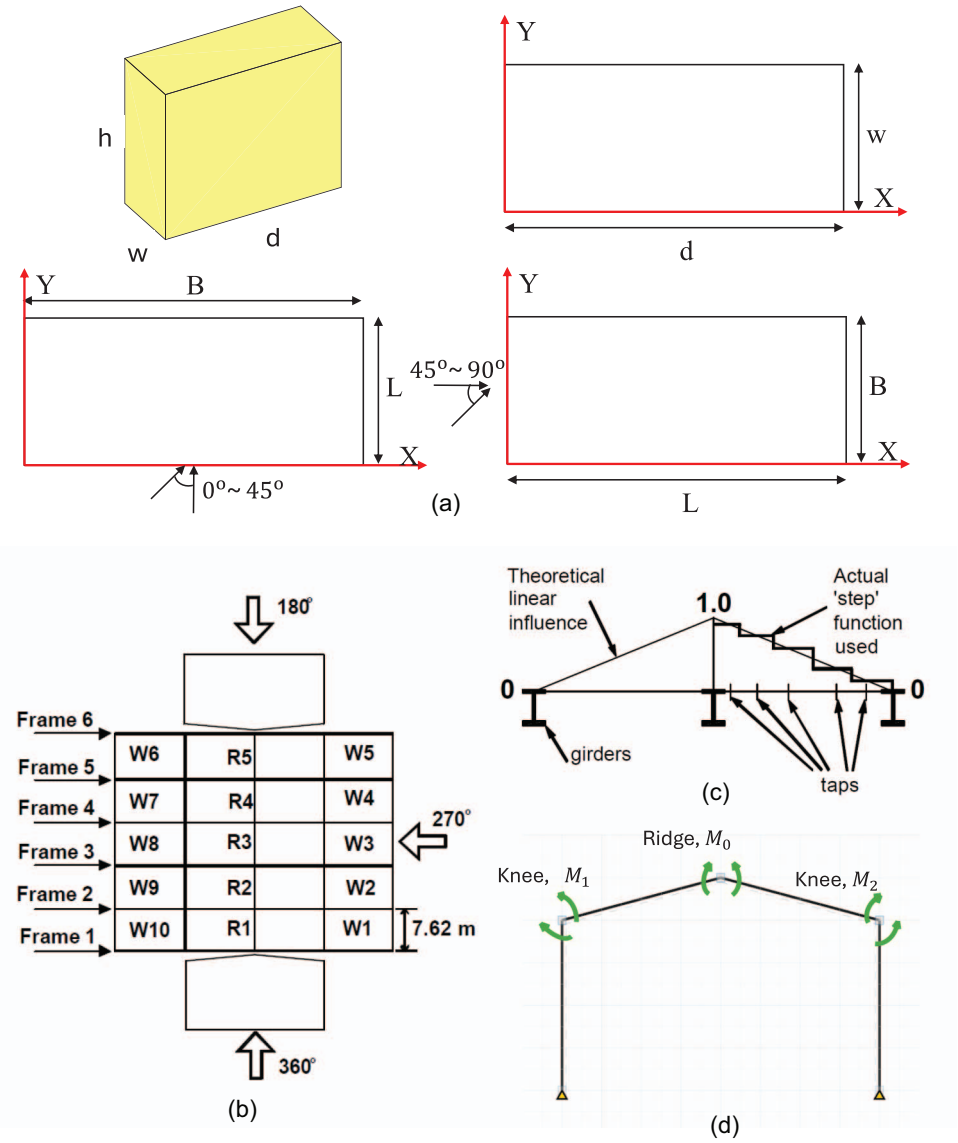

Fig. 2. (Color) (a) Definition of coordinate system; (b) bay and frame spacing for a low-rise structure; (c) linear influence functions between the girders of a frame; and (d) two-pin moment-resisting frame and the joint moments.

parameters then were converted to a 1-h (3,600-s) duration (at full scale) using the equations developed by Cook and Mayne (1979). Peak values corresponding to a 57% probability of nonexceedance (the expected value of a Gumbel distribution) then were calculated. These steps were applied to each response for each building for every wind direction. Fig. 3 provides one example of a peak coefficient for one response—in this case, the roof uplift—for one building as a function of wind direction. The single worst value among all wind directions was identified from these; in Fig. 3, it is the value at the wind direction of 270°. The resulting peak responses for each building are called target responses because they are the critical values for determining the design values.

Method to Determine Design Pressure Coefficients and Pressure Zones

Equivalent Peak Pressure Distributions

To identify the patterns associated with the target responses, such as that in Fig. 3, the load response correlation (LRC) method, developed by Kasperski and Niemann (1992), was adopted. Without a loss of generality, the peak pressure can be written

$$Cp_{\mathrm{LRC},i} = \overline{Cp_i} + g\rho_{i,r}\sigma_{Cp_i} \tag{1}$$

where $\overline{Cp_i}$ and σ_{Cp_i} = mean and standard deviation of a point pressure coefficient referenced to the mean dynamic pressure at the mean roof height; i = index of pressure tap; $\rho_{i,r}$ = correlation coefficient between the time series of $Cp_i(t)$ and the load response coefficient, $r(t)$; and g = peak factor of the response $r(t)$. The peak factor is calculated as

$$g = \frac{\hat{r} - \bar{r}}{\sigma_r} \tag{2}$$

where $\hat{r}$, $\bar{r}$, and σ_r = peak, mean, and standard deviation of $r(t)$, respectively. The resulting term, $Cp_{\mathrm{LRC},i}$, can be viewed as an equivalent peak pressure coefficient distribution associated with the target response, which will always satisfy

$$\sum_{i=1}^{n} Cp_{\mathrm{LRC},i} IA_i = \hat{r} \tag{3}$$

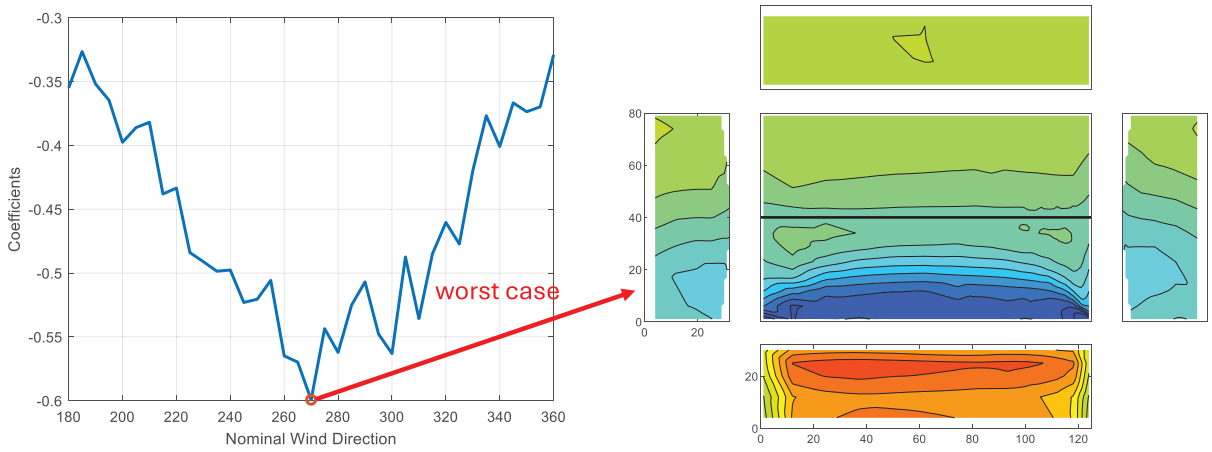

Fig. 3. (Color) Contour plot of Cp_{LRC} for the worst-case uplift coefficient for a selected NIST model.

where $\boldsymbol{I}$ = influence function associated with the particular response. For each structural response of interest, the peaks are calculated for each wind direction following the approach discussed in section "Peak Responses." The patterns of equivalent peak pressure distributions are determined for the largest magnitude peak, depicted by contour plots of the Cp_{LRC} data. One example is shown in Fig. 3, where the Cp_{LRC} contours are shown as an exploded view of the building surfaces. The roof is in the center, with the ridge shown as a solid black line and the four walls shown adjacent to the appropriate roof edge. These Cp_{LRC} contours are obtained for every target response for every building in the database. In total, 1,537 contour plots were developed, covering the 85 buildings in the three databases, the two terrain simulations, and the range of responses considered.

Identification of Spatial Pressure Patterns

The Cp_{LRC} contour plots were examined to identify the patterns associated with the pressure coefficients that led to the target responses. This revealed that most of the spatial pressure distributions associated with the critical reactions can be represented by a few typical patterns. Fig. 4 provide examples for a low-rise building with a low-slope roof.

All the data for buildings with low-sloped roofs indicated that most of the Cp_{LRC} distributions can be categorized into three typical patterns: (1) Pattern 1 has wind nominally parallel to the ridge (x-direction), with large suctions on the roof near the windward gable edge, relatively uniform pressure distributions on the windward (positive) and leeward (negative) walls, and sidewalls that are similar to those on the roof; (2) Pattern 2 has wind nominally perpendicular to the ridge (y-direction), with large suctions on the roof near the windward eaves edge, and walls with similar patterns as in Pattern 1; and (3) Pattern 3 has wind approaching from an oblique direction, with a conical vortex pattern on the roof, positive pressures on the windward walls with close to a uniform gradient, and relatively uniform suction on the leeward walls. Fig. 4 shows the typical patterns of Cp_{LRC} distributions associated with a series of responses for a low-rise building model from the NIST database with a roof slope of 1:12, and geometric parameters of $d \times w \times h = 125 \times 80 \times 40$ ft. These three pattern can be identified clearly in the figure. Similar patterns were observed for mid-rise and high-rise models with flat roofs; further examples were presented by Guo et al. (2024), but are not included here for brevity.

Figs. 5(a, b, and c) show the typical patterns of Cp_{LRC} distributions for 6:12 sloped gable-roof buildings with $h/w = 0.5$ and $d/w = 2$. As with the low-sloped-roof buildings, three typical patterns can be identified. For wind nominally perpendicular to the gable end (x-direction), the pressure distribution patterns are similar to Pattern 1 of the low-sloped-roof buildings [Figs. 5(a) and 4]. For wind nominally perpendicular to the ridge (y-direction), the pressure distribution patterns on the walls are similar to Pattern 2 of the low-sloped-roof buildings, but the roof patterns are different: positive pressures on the windward roofs and uniform suction on the leeward roofs [Figs. 5(b) and 4]. Compared with the low-sloped-roof buildings, more responses are controlled by the oblique direction wind for the 6:12 sloped model. The pressure distribution patterns on the walls are close to Pattern 3 of the low-sloped-roof buildings. However, the patterns on the roof are more complicated: the positive pressure contours on the windward roof and the suction contours on the leeward roof are irregularly shaped and not well suited for modeling as simple rectangular zones [Fig. 5(c)].

Figs. 5(d, e, and f) depict the typical patterns of Cp_{LRC} distributions of a 6:12 sloped hip roof building with $h/w = 0.5$ and $d/w = 2$. Compared with the gable roof models, the wall patterns are similar, while the roof patterns are different. For wind from the x- and y-directions, low suctions occurs on the side roof behind the hip lines; for wind from the oblique directions, irregularly shaped pressure distributions are observed on all roof surfaces. Results of Cp_{LRC} distributions associated for several critical responses are presented in the Appendix.

Area-Averaged Pressure Coefficients for the Target Responses for Each Building Zone

Following the identification of the pressure patterns, Fig. 1 indicates that the next step in the method (Step 5) is to identify and propose zones of constant pressure on each building surface (for each target response for each building). Fig. 6 presents one example, showing the zone patterns overlayed on a contour plot of pressure coefficients similar to that in Fig. 3. Fig. 6 provides a schematic of initial zones on top of the actual point pressure coefficients. After the zone shapes and sizes are proposed, the pressure coefficients for each zone corresponding to a peak response can be calculated (Fig. 1, Step 6) via

$$Cp_A = \frac{\iint Cp_{\mathrm{LRC}} I ds}{\iint I ds} \tag{4a}$$

where I = influence function; and ds = area. This integration guarantees that for the reaction, the net contribution from each zone is unchanged.

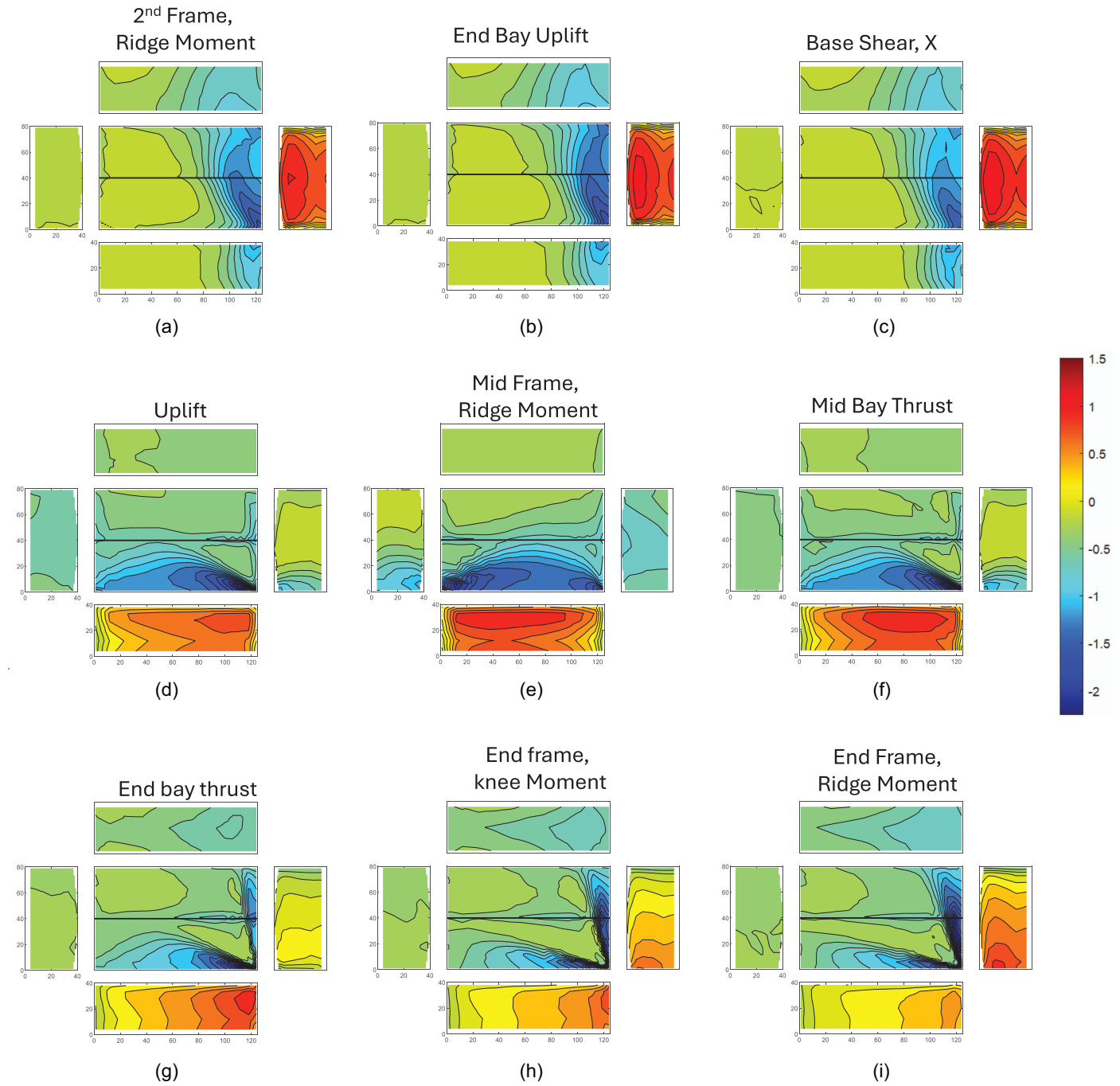

Fig. 4. (Color) Examples of typical patterns of Cp_{LRC} distribution associated with critical structural responses for a 1:12 sloped roof low-rise building, $d \times w \times h = 125 \times 80 \times 40$ ft.

For zones where the influence function is zero, it is still useful to understand what the pressures are because the goal is to obtain realistic patterns. In this case, Cp_A is calculated as the simple area average

$$Cp_A = \frac{\iint Cp_{\mathrm{LRC}} d\boldsymbol{s}}{\iint d\boldsymbol{s}} \tag{4b}$$

The integrated Cp_A (except for the windward wall) then is converted to $[GCp]$ via

$$GCp = \frac{Cp_A}{(1 + g_u I_u)^2} \tag{5a}$$

where g_u and I_u = peak factor and turbulence intensity of the reference velocity, respectively. Details of the selection of the velocity parameters for the 3-s gust speeds were presented by Acosta et al. (2024.) For the windward wall only, the $[GCp]$ values are calculated as

$$[GCp] = \frac{\iint Cp_{\mathrm{LRC}} \boldsymbol{I} d\boldsymbol{s}}{(1 + g_u I_u)^2 \iint \boldsymbol{I} \cdot \boldsymbol{I}_R d\boldsymbol{s}} \tag{5b}$$

where $\boldsymbol{I}_R$ is a rereferencing function of height, z

$$\boldsymbol{I}_{R,z} = \left(\frac{V_{3-s,z}}{V_{3-s,h}}\right)^2 \tag{6}$$

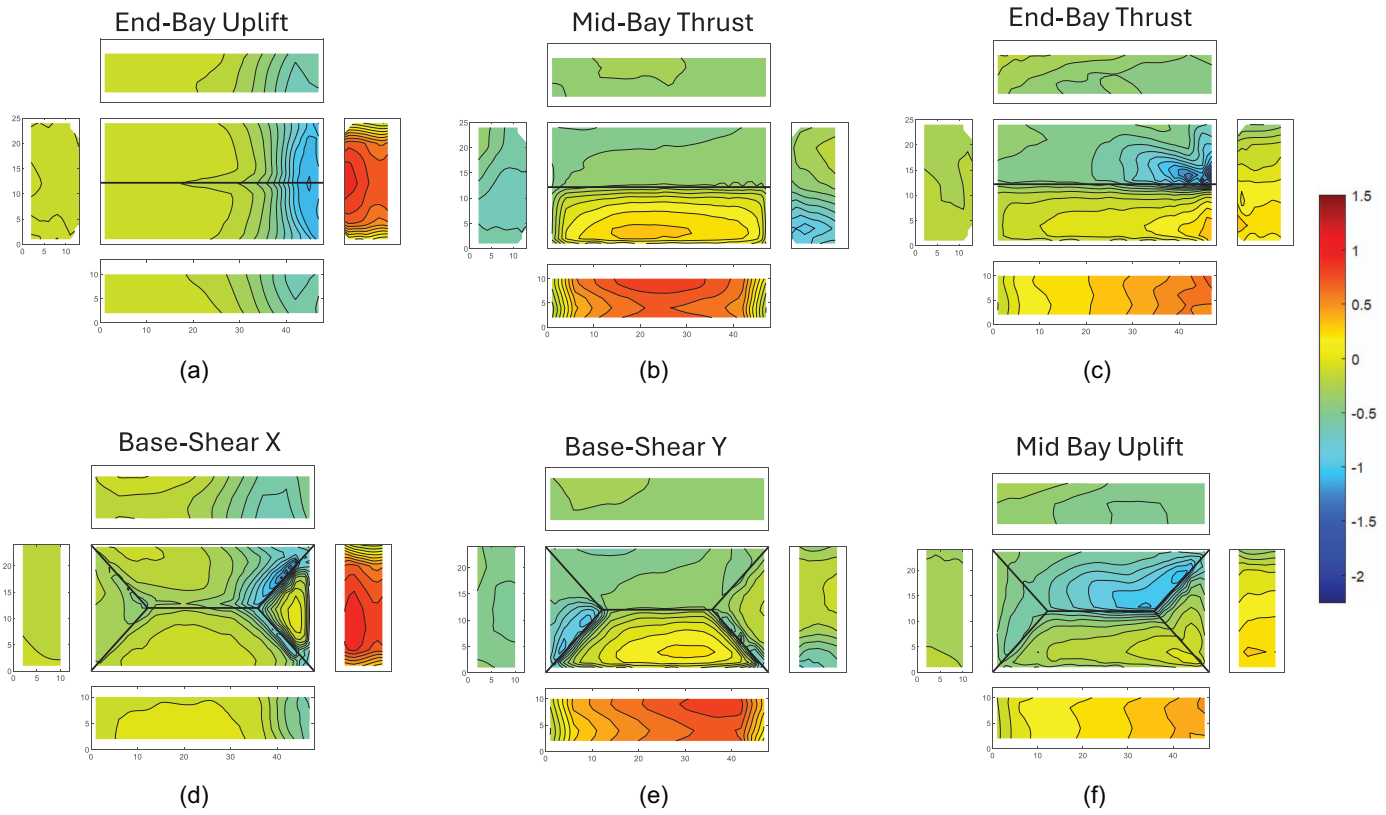

Fig. 5. (Color) Examples of typical patterns of Cp_{LRC} distribution associated with critical structural responses for low-rise buildings with 6:12 sloped roofs, $d \times w \times h = 48 \times 24.38 \times 12.19$ m: (a, b, c) gable; and (d, e, f) hip.

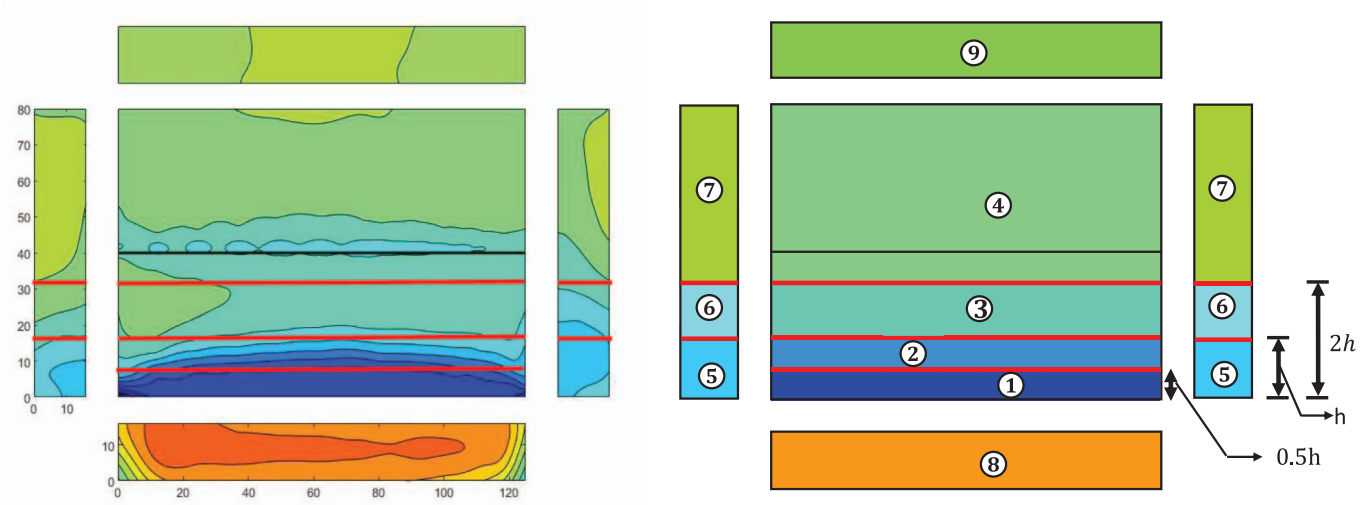

Fig. 6. (Color) Schematic of GCp integrated zones from the initial Cp_{LRC} distribution.

where $V_{3-s,z}$ and $V_{3-s,h}$ = 3-s gust velocities at the local and mean roof heights, respectively. For windward walls, the integration in Eq. (5*b*) ensures that the calculated GCp value leads to correct peak loads when applied with velocity referenced to the local height (instead of the mean roof height), as in ASCE 7.

At this stage, Step 6 in Fig. 1 yields a set of pressure coefficients and zones sizes for each target response. These are different for each target responses, although there is reasonable similarity, as implied by the similarity in the patterns in Figs. 4 and 5. The next stage in the process is to determine a single set of pressure coefficients and zones for each building.

Optimized Pressure Coefficients for Each Building

Because there are so many target responses for each building, we introduce the term best single response. The best single response is one that (1) closely represents the pressure pattern, and (2) is for a reaction that is deemed to have a relatively higher importance level. For example, for the roof zones, the best single responses typically are overall uplift or a bay uplift. For the wall zones, they generally are the base-shear for windward and leeward walls, and area-averaged suction for the sidewalls. Further details of best single responses for each zone were presented by Guo et al. (2024).

J. Struct. Eng., 2025, 151(11): 04025182

The ideal pressure coefficients should provide values that minimize the errors for all the different target responses. To achieve that, an optimization method was developed based on a gradient descent algorithm, which minimizes the total difference between the calculated response values and those from the measured wind tunnel data.

The gradient descent algorithm works as follows. For a load case with m different zones, the surface pressure distribution, $\boldsymbol{p}$, can be written as a function of $[GCp]$ values of each zone:

$$\boldsymbol{p} = \boldsymbol{p}([GCp_1], [GCp_2], \ldots, [GCp_m]) \tag{7}$$

A total of n peak responses, $\hat{r}_1, \hat{r}_2, \ldots, \hat{r}_n$, are governed by this load case, as identified from section "Identification of Spatial Pressure Patterns," with the corresponding influence functions $I_1, I_2, \ldots, I_n$.

For a given set of $\boldsymbol{p}$ obtained from the Cp_{LRC} distributions of a particular response, the previous responses can be calculated from the following integration:

$$\begin{bmatrix} \hat{r}'_1 \\ \hat{r}'_2 \\ \vdots \\ \hat{r}'_n \end{bmatrix} = \iint \boldsymbol{p}(GCp_1, GCp_2, \ldots, GCp_m) \begin{bmatrix} \boldsymbol{I}_1 \\ \boldsymbol{I}_2 \\ \vdots \\ \boldsymbol{I}_n \end{bmatrix} \boldsymbol{I}_R d\boldsymbol{s} \tag{8}$$

where $\boldsymbol{I}_R$ = rereferencing function defined by surface location, as discussed previously. For windward walls, $\boldsymbol{I}_R$ is defined by Eq. (6); for other surface locations, $\boldsymbol{I}_R$ equals 1.

The relative error can be calculated as

$$\epsilon_i = (\hat{r}'_i - \hat{r}_i)/\hat{r}_i \tag{9}$$

The purpose of the optimization is to minimize ϵ_i.

The cost function is defined as the weighted average of the relative error square

$$C = \sqrt{\frac{\sum_{i=1}^{n} (w_i \epsilon_i)^2}{n}} \tag{10}$$

where w_i = weight function defined to account for the different importance level of each response. In this study, for low-rise models, the weight functions for joint moments, overall force, and bay uplift and thrust were set to be 1, 2, and 3, respectively; for mid- and high-rise models, the weight functions of overall reactions were set to 1, whereas for floor-to-floor shear they were set to $1/N$, where N is the number of floors. The cost function is minimized gradually using iteration

$$GCp_j^{(k+1)} = GCp_j^k - \alpha \times \frac{\partial C}{\partial GCp_j} \tag{11}$$

where α is a parameter controling the convergence speed (referred to as the learning rate in machine learning), determined by each specific case.

The initial values of the iteration are important to prevent the iteration from falling into a false local optimal solution, and are obtained from the averaged zone $[GCp]$ of the best single response of each zone.

The optimization is applied to each building individually, resulting in an optimum set of pressure coefficients for each pattern on each building. (For the models with 6:12 sloped roofs, more than one value is required for the windward roof zone; details are presented in section "Synthesis of Pressure Coefficients for All Buildings." This creates additional complexity for the optimization method. Thus, the $[GCp]$ of the best single responses are taken directly to represent the optimum pressure coefficients.) The synthesis of the optimum coefficients from all buildings, which is Step 7 in Fig. 1, is discussed in the following section.

Synthesis of Pressure Coefficients for All Buildings

To develop a method for all buildings, the optimum set of pressure coefficients and zones for each building must be brought together into a framework for all buildings. This is achieved by using the concept of nondimensional building geometric parameters that control the aerodynamic loading as a function of the building shape. These critical parameters were determined previously by Wang and Kopp (2021a, b). We used those parameters to create zone sizes that depend on the critical building dimensions for the particular building surface (Fig. 7). All the pressure coefficients for the 85 building shapes were plotted for each zone as a function of the critical nondimensional geometric parameters. These data are shown in Figs. 8 (for roofs) and 9 (for walls). Fits were made of the data to provide the final design values of the pressure coefficients. These fitted models were adjusted slightly using a trial-and-error procedure to improve the overall model performance (Section "Validation of the New Proposed Pressure Coefficients").

The final optimized pressure zones are provided in Fig. 7, and are generally based on Patterns I and 2. For low-sloped roofs, four zones are proposed for the roof with three zones on the side walls to capture the high suction loads near the windward edges. The zone sizes are defined by the minimum of either the building breadth, B (Fig. 2) or the mean roof height, h, based on the analysis by Wang and Kopp (2021a, b). There is one zone on the windward wall and one zone on the leeward wall, due to their approximately uniform pressure distributions. For gable roofs with slopes greater than 2:12, for wind parallel to the ridge (x-direction), the pressure patterns on the roof (Pattern 1) are similar to those for low-slope roofs and are maintained. For wind perpendicular to the ridge (y-direction), one zone was developed for the windward roof and one zone was developed for the leeward roof. For hip roofs, there is a great deal of complexity in terms of the building shape parameters that control roof pressure zones. Thus, for simplicity, it was decided that the pressure patterns for gable roofs would be used for hip roofs along the ridge direction, as currently is the case in ASCE 7. The implications of this are examined subsequently.

The oblique wind direction pattern (Pattern 3) was not required because it controlled few target responses (although it notably controlled torsion). In the interests of simplicity, the pattern was removed in favor of the use of an eccentricity to obtain torsional responses. This is consistent with what is currently used for the load cases for the directional procedure in Chapter 27 of ASCE 7-22. Details of the load cases are discussed in the next section.

Fig. 8 presents all the data and the final curve fits for roofs, and Fig. 9 presents these for the walls. For all pressure coefficients on the roof, the nondimensional parameter used for fitting is $\min(B, h)/L$, where B and h represents the building breadth and height, respectively, and the smaller of the two is taken as the critical building dimension for roof aerodynamic loads. For low-rise structures, for wind perpendicular to the wall, the bulk of the approaching wind flow goes over the roof, separating at the windward wall edge. As a consequence, building height is critical for describing the flow field, and the nondimensional parameter h/L works well for capturing the trend of pressure versus building shapes for the suction loads on roof, as well as leeward and side walls (Wang and Kopp 2021a). For high-rise structures, in contrast, the bulk of the approaching wind flow tends to flow around the side walls instead of over the roof, making the building breadth the critical dimension, and the best nondimensional parameter is

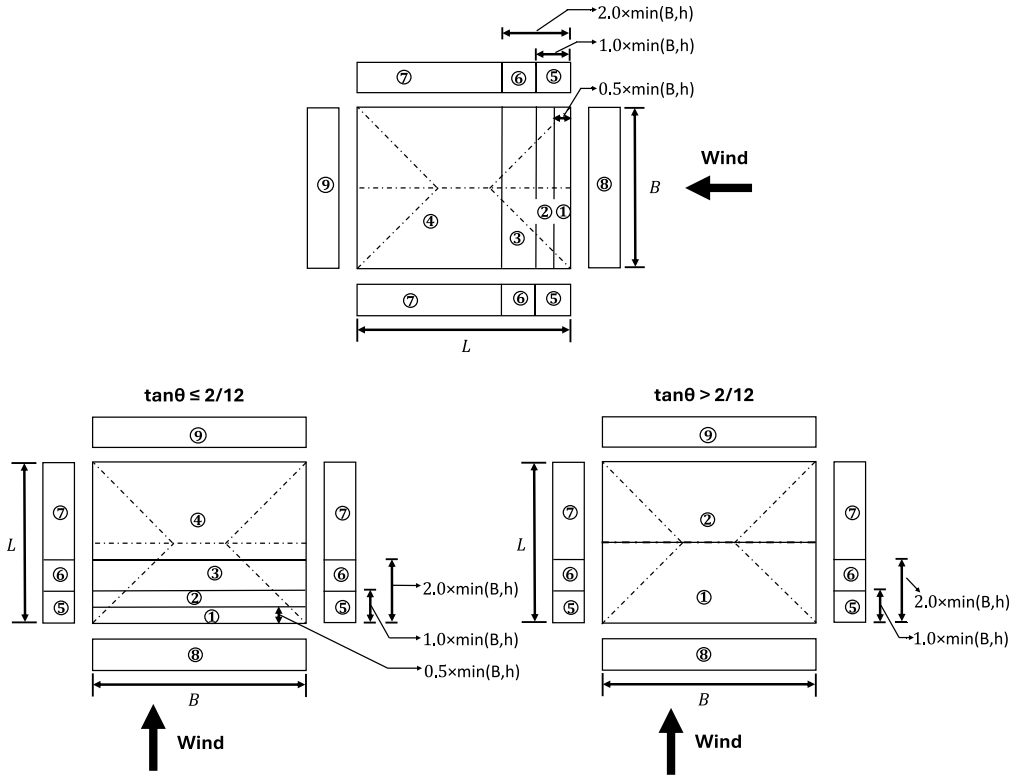

Fig. 7. Final version of proposed pressure zones.

B/L (Wang and Kopp 2021a, b, c). For the windward section of 6:12 sloped roofs for wind perpendicular to the ridge [Fig. 8(c)], the windward roof patterns are complex. This results in two curves to estimate different responses—one for the positive horizontal load, and one for the negative (i.e., uplifting) vertical loads.

Fig. 9 depicts the data for the walls. For windward walls, the best nondimensional parameter to capture the trend of loading versus building shape is h/B, due to the nature of the horseshoe vortices that control the local aerodynamics near the windward wall surfaces (Wang and Kopp 2021c). For leeward walls, the best nondimensional parameter is h/L for low-rise shapes (that satisfy $h/w < 1$) and B/L for high-rise shapes ($h/w \geq 1$). For both windward and leeward walls, multiple curves are necessary to capture the difference between buildings with different h/w values. For the sidewalls, the nondimensional parameter is $\min(B, h)/L$, which is consistent with the roof zones.

In general, the optimized coefficients for each building provide reasonable similarity for the patterns and pressure coefficient magnitudes (Figs. 8 and 9). This is attributed to the fact that the overall nondimensional building geometry parameters are effective at reducing the variation in the aerodynamic coefficients, as discussed by Wang and Kopp (2021a, b, c). This also suggests that the zone sizes, and their normalizations, are reasonably effective at capturing the variation of the pressures on each surface for the critical reactions. The effects of the variation in the pressure coefficient values, which are clear in Figs. 8 and 9, on the overall MWFRS loads are examined in section "Validation of the New Proposed Pressure Coefficients," which provides validation.

The directional and envelope procedures of ASCE 7 each have distinct load cases, which tell the user how to apply the pressures to the building surfaces. Because the directional procedure applies to buildings of all heights, whereas the envelope procedure applies only to low-rise buildings, it was decided to utilize the load cases from the directional procedure (ASCE 7-22, Fig. 27.3-8) as the basis for the unified method. Generally, these load cases effectively capture the target responses. However, some modifications are necessary (Fig. 10).

These modifications primarily result from conflicting choices that had to be made in optimization of the pressure coefficients and building zones. For example, the base shear and bay thrust for low-rise buildings lead to such a conflict. The bay thrust for low-rise buildings was captured by Pattern 3 (Fig. 4), whereas the overall base shear was captured by Patterns 1 (for the x-direction) and 2 (for the y-direction). This issue could have been handled three ways: (1) by including another set of pressure zones, such as a simplification of those in Pattern 3; (2) by increasing the pressure coefficients for Patterns 1 and 2 so that the bay thrust was matched, but at the cost of overall base shears that are too large; or (3) by altering Load Case 3. Increasing the base shear to inaccurate values clearly is not desirable, so the two alternatives were adding the third pressure pattern for cornering winds or modifying Load Case 3 to account for this. It was decided to modify Load Case 3 as the simplest outcome, particularly because Load Case 2 was an excellent model for the torsional loads, eliminating the need for Pattern 3 to account for that.

Fig. 10(c) shows the existing Load Case 3, which was maintained, and is labelled Load Case 3(1). Fig. 10(d) shows the modification, labelled as Load Case 3(2). Case 3(2) brings increased loading at the wall corner zones, with a 175% increase of the windward pressure and 100% leeward pressure from Load Case 1 [Fig. 10(a)]; for the rest of the wall, it requires the same windward wall pressures of the original Load Case 3 (i.e., 75% of Case 1), but zero pressures on the leeward walls. The size of the corner zone (a_x, a_y) is taken as the smaller of $2h$ and $0.3B$ in the corresponding direction. Additionally, for Load Case 2, the eccentricity model was updated to more accurately account for the full range of building heights (Guo et al. 2024).

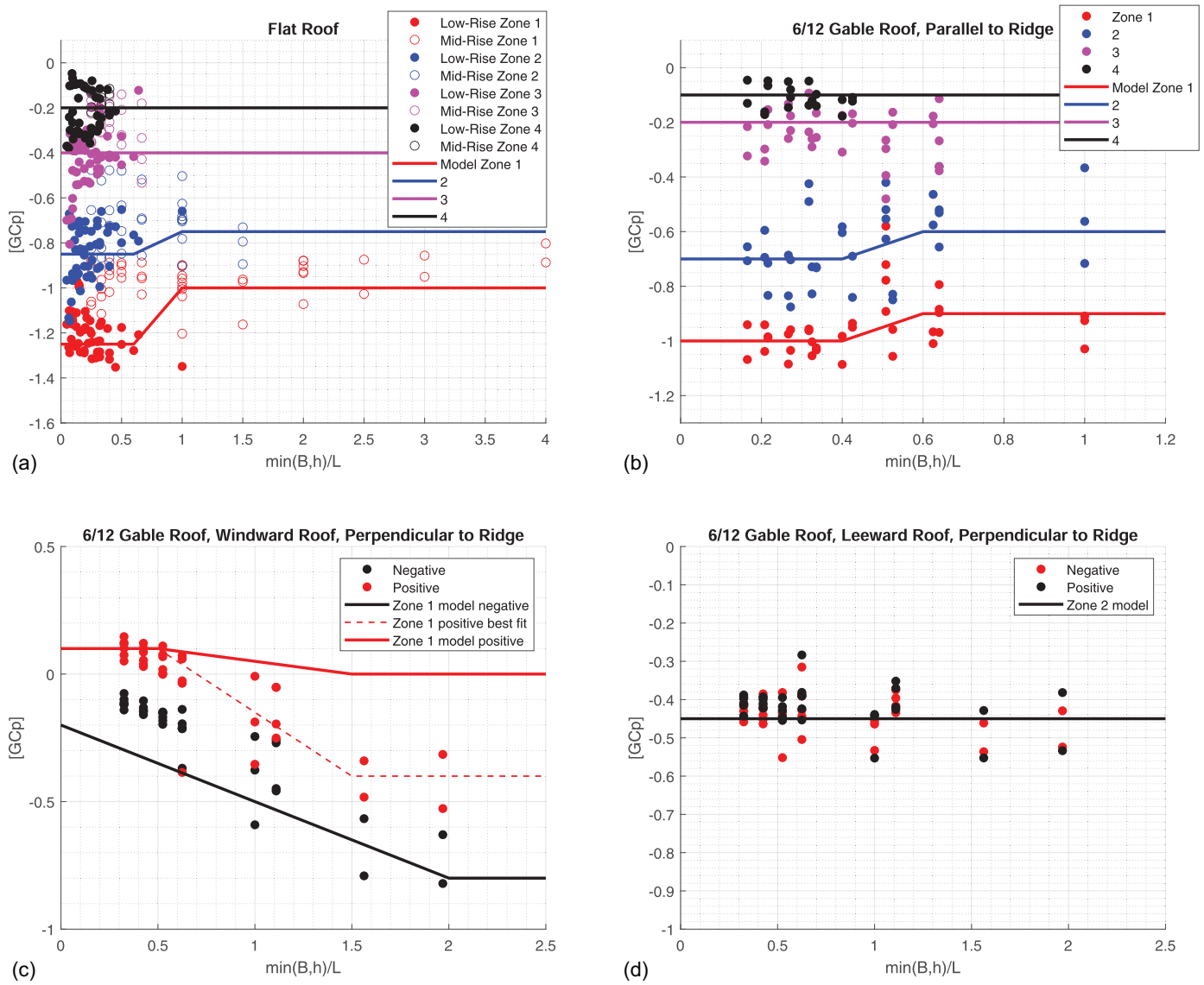

Fig. 8. (Color) *GCp* data for each building along with the model fit for (a) Zones 1–4 for low-sloped roofs; (b) Zones 1–4 for 6:12 sloped roofs for wind parallel to ridge; (c) Zone 1 (windward roof) for 6:12 gable roofs for wind perpendicular to ridge; and (d) Zone 2 (leeward roof) for 6:12 gable roofs for wind perpendicular to ridge.

Validation of the New Proposed Pressure Coefficients

To validate the final proposed recommendations, the structural responses were calculated from the proposed model and compared to the values of the target responses from the wind tunnel data. Model results were enveloped using the modified load cases described previously. Results for several responses are presented in Figs. 11–13; the full set of results was presented by Guo et al. (2024). In Figs. 11–13, the proposed model values are presented on the vertical axis, and the experimental values are presented on the horizontal axis. A perfect model would be a 45° straight line on these plots. In other words, the closer the variation and scatter are to the 45° line, the better is the model. In general, the goal is to have limited bias such that the scatter is on either side of the 45° line and within a reasonably narrow range such that no building has measured reactions that are substantially different from those of the proposed model. Results calculated from ASCE 7-22 Chapters 27 and 28 are included for comparison. For Chapter 27, the gust effect factor is taken as 0.85 because rigid buildings are assumed for the development of these pressure coefficients. In general, the results from the proposed model are much better at matching the experimental data and capturing the basic aerodynamic trends than the existing provisions.

For buildings with low-sloped roofs, for overall horizontal forces {i.e., base shears in both directions [Figs. 11(c) and 12(a)], and overturning moments for mid and high-rise buildings [Fig. 12(c)]}, the new model matched the experimental data reasonably well. In contrast, Chapter 27 generally tends to overestimate these loads for low-rise buildings and tends to underestimate the loads for mid- and high-rise buildings. Chapter 28 fails to capture the variation in wind load coefficients with building geometry. Significant improvements are evident for the overall uplift [Figs. 11(a) and 12(b)], end-bay uplifts [Fig. 11(b)], and the sidewall suctions for mid- and high-rise buildings [Fig. 12(f)] because the existing provisions generally underestimate the loads. The torsional loads were calculated using the horizontal forces from the proposed pressure coefficients together with an updated eccentricity model. The results

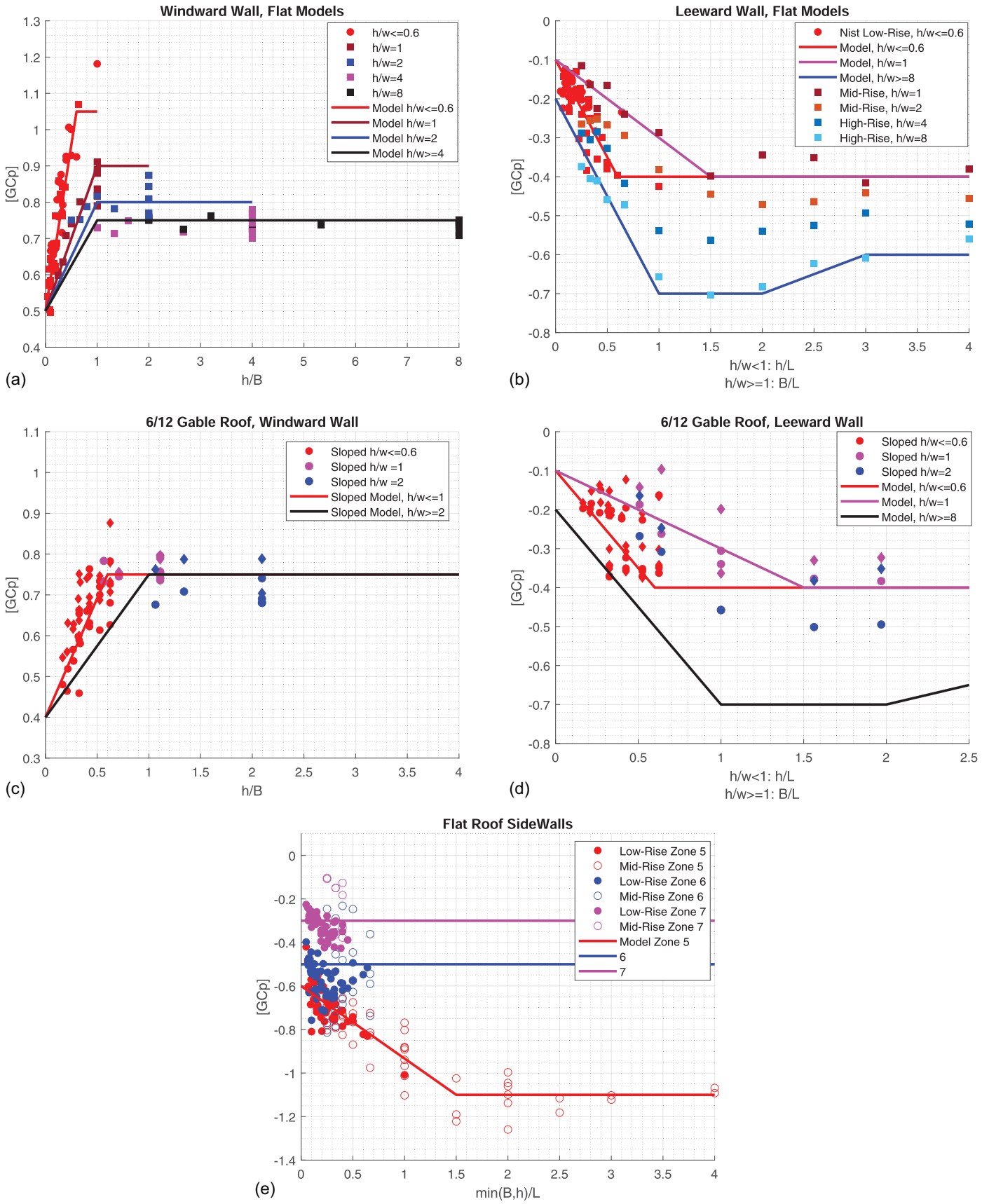

Fig. 9. (Color) *GCp* data for buildings with (a) low-sloped roofs, Zone 8 (windward walls); (b) low-sloped roofs, Zone 9 (leeward walls); (c) 6:12 gable roofs, Zone 8 (windward walls); (d) 6:12 gable roofs, Zone 9 (leeward walls); and (e) low-sloped roofs, Zones 5–7 (sidewalls).

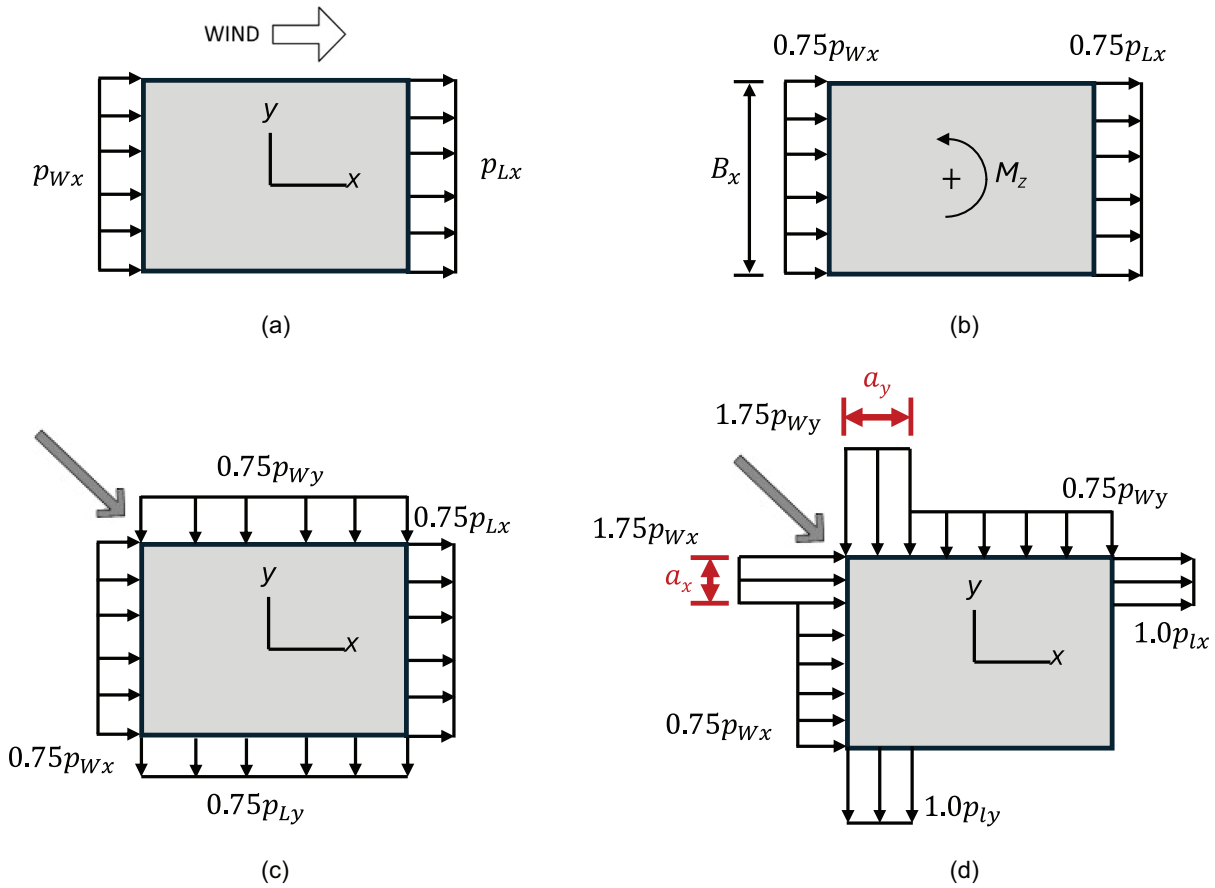

Fig. 10. (Color) Schematic sketches of the final proposed load cases: (a) Load Case 1 (x-direction only), (b) Load Case 2 (x-direction only), (c) Load Case 3(1), and (d) Load Case 3(2).

captured the trend of the experimental data well [Fig. 11(e) and 12(e)].

For the end-bay thrusts [Fig. 11(d)] and the end-frame ridge moments [Fig. 11(f)], the proposed provisions work sufficiently well, and are significantly better than the existing values because Chapters 27 and 28 tend to underestimate the loads. These reactions are controlled mostly by the oblique wind direction pattern. As discussed previously, the oblique-wind-direction Pattern 3 was removed during the simplification process. Instead, the wall corner zone in the newly proposed Load Case 3(2) helps to capture the reactions governed by this pattern.

For the buildings with 6:12 sloped gable and hip roofs, the results from the proposed models match the experimental data well for the overall forces {uplifts, base shears, and torsions [Figs. 13(a, c, and e)]}, and are mostly an improvement on the current provisions. Torsion for buildings with $d/w = 1$ and $h/w \leq 1$ are not shown in Fig. 13 because they are mostly exempted from torsional design. The model provides overly conservative results for these buildings.

As for the low-sloped roofs, the proposed models work well for the end-bay uplift for gable roofs [Fig. 13(b)]. This is a significant improvement on the current provisions because the current provisions underestimate these loads. For the hip roofs, the new model is conservative (i.e., safe). Improvements also are evident for end-bay thrusts [Fig. 13(d)] and the end-frame ridge moments [Fig. 13(f)].

The proposed model works better for gable roofs than for hip roofs (Fig. 7). This is not surprising, because the pressure coefficients and zone shapes and patterns were developed primarily from the gable roof data, and hip roofs are treated like gable roofs for the along-the-ridge wind direction, as in the existing provisions. This approach directly leads to the conversative results for the end-bay uplift of hip roofs, which is controlled by the low-suction areas on the roof side surfaces behind the hip lines [Figs. 5(d and e)]. Those areas are not captured by the current model due to the limitation of the data available and considerations for simplicity in the zones. The authors attempted a wide range of zone shapes, zone sizes, and approaches to each of these, and the results indicated that additional load cases would be required beyond simple re-zoning of the current proposed model or simple changes to the existing load cases. Additionally, any further optimization would require significant additional wind tunnel data to cover many more building geometries (in particular, for both roof slopes and plan shapes and dimensions), as well as more-complex zoning, which likely would become more like the component and cladding zones for hip roofs in Chapter 30 of ASCE/SEI 7 (ASCE 2022).

Conclusions

This paper presents a method for obtaining aerodynamic coefficients and load cases for a unified set of MWFRS provisions. The proposed provisions are based on a combination of the directional and envelope procedures. The coefficients were developed based on the rigid building assumption, and the resonant component of the structural response is not included or assessed. Three groups of wind

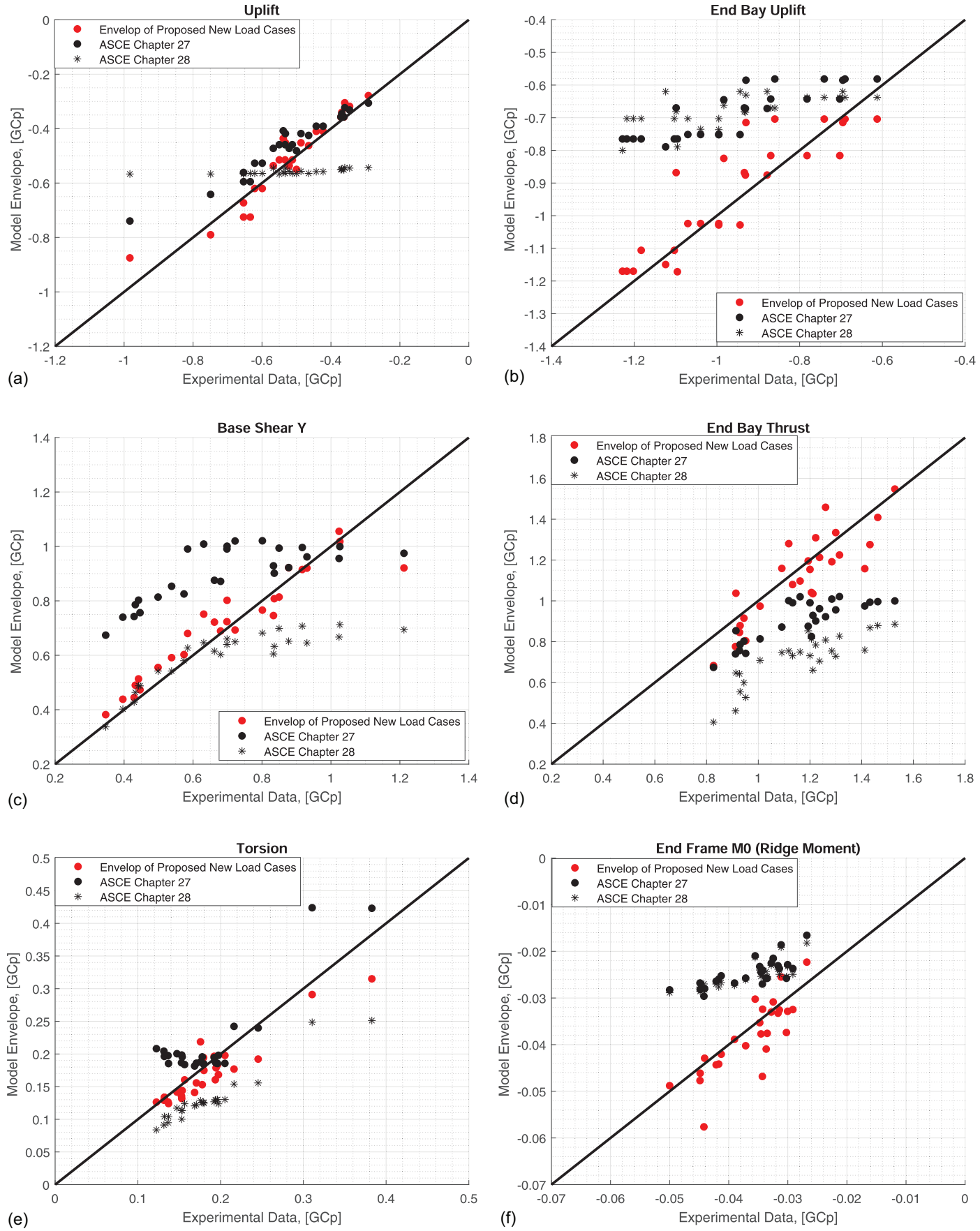

Fig. 11. (Color) Measured and modeled results for low-sloped, low-rise buildings.

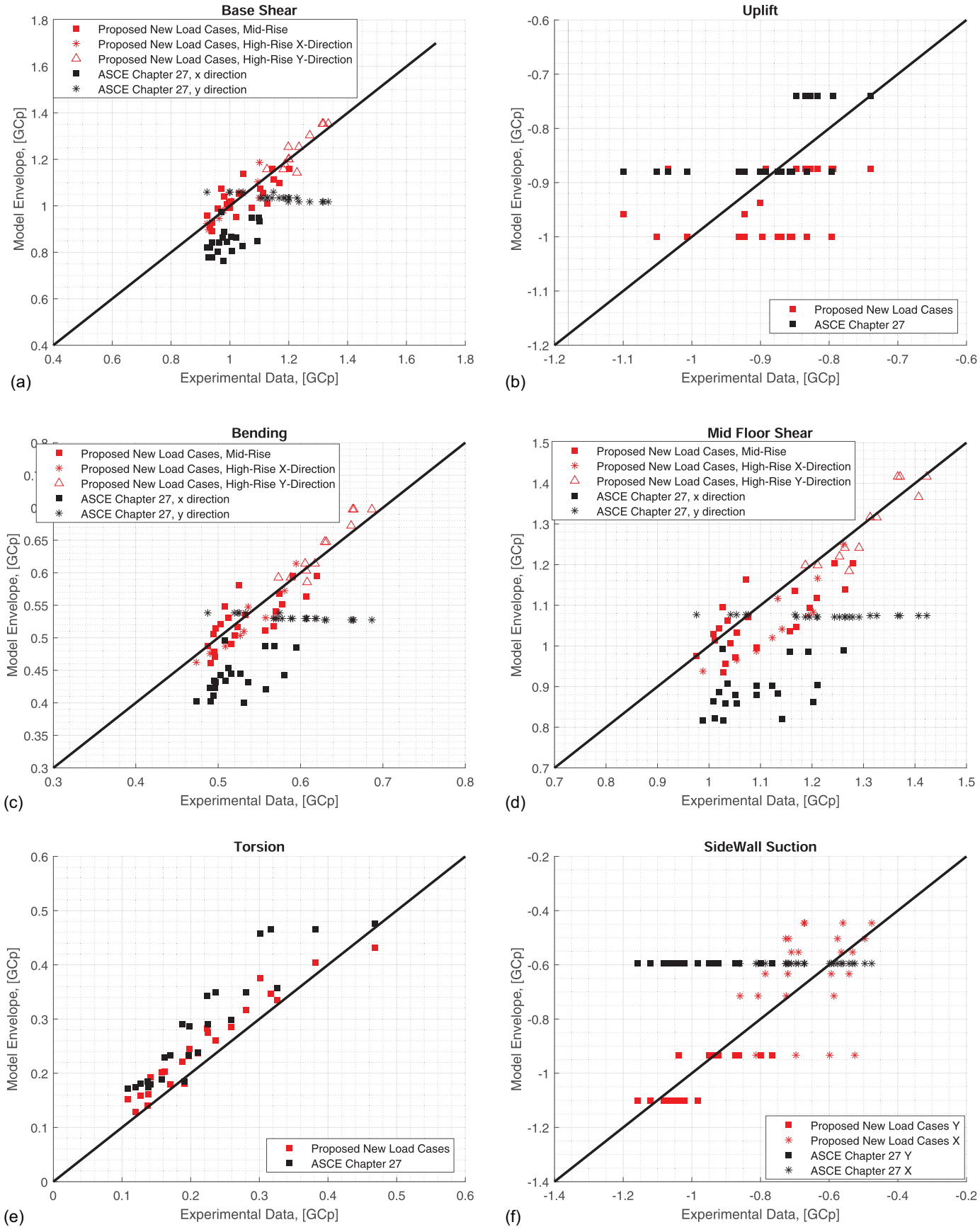

Fig. 12. (Color) Measured and modeled results for low-sloped, mid and high-rise buildings.

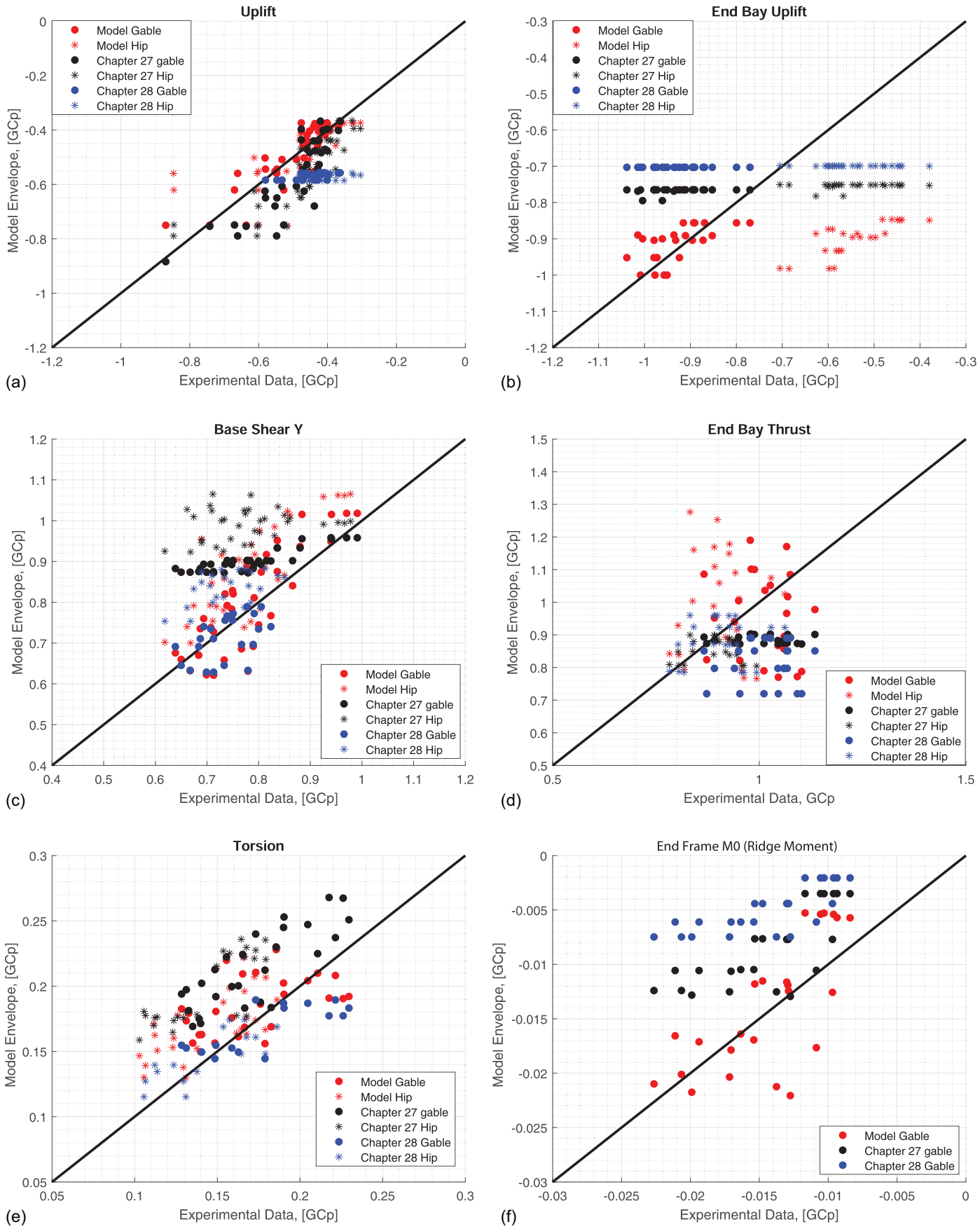

Fig. 13. (Color) Measured and modeled results for 6:12 sloped gable and hip roof buildings.

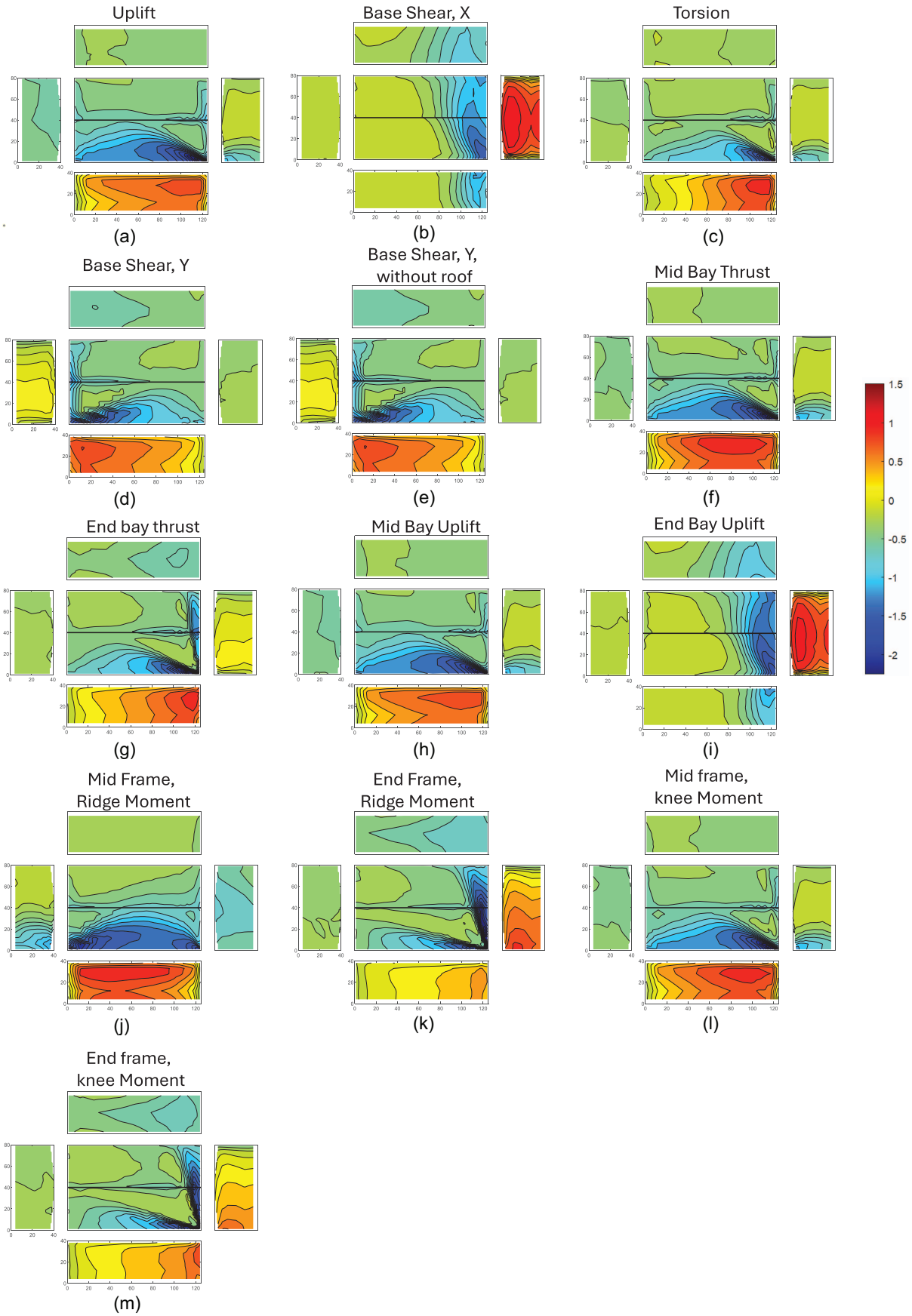

Fig. 14. (Color) Typical Cp_{LRC} distribution associated with critical structural responses for a 1:12 sloped roof low-rise building, $d \times w \times h = 125 \times 80 \times 40$ ft.

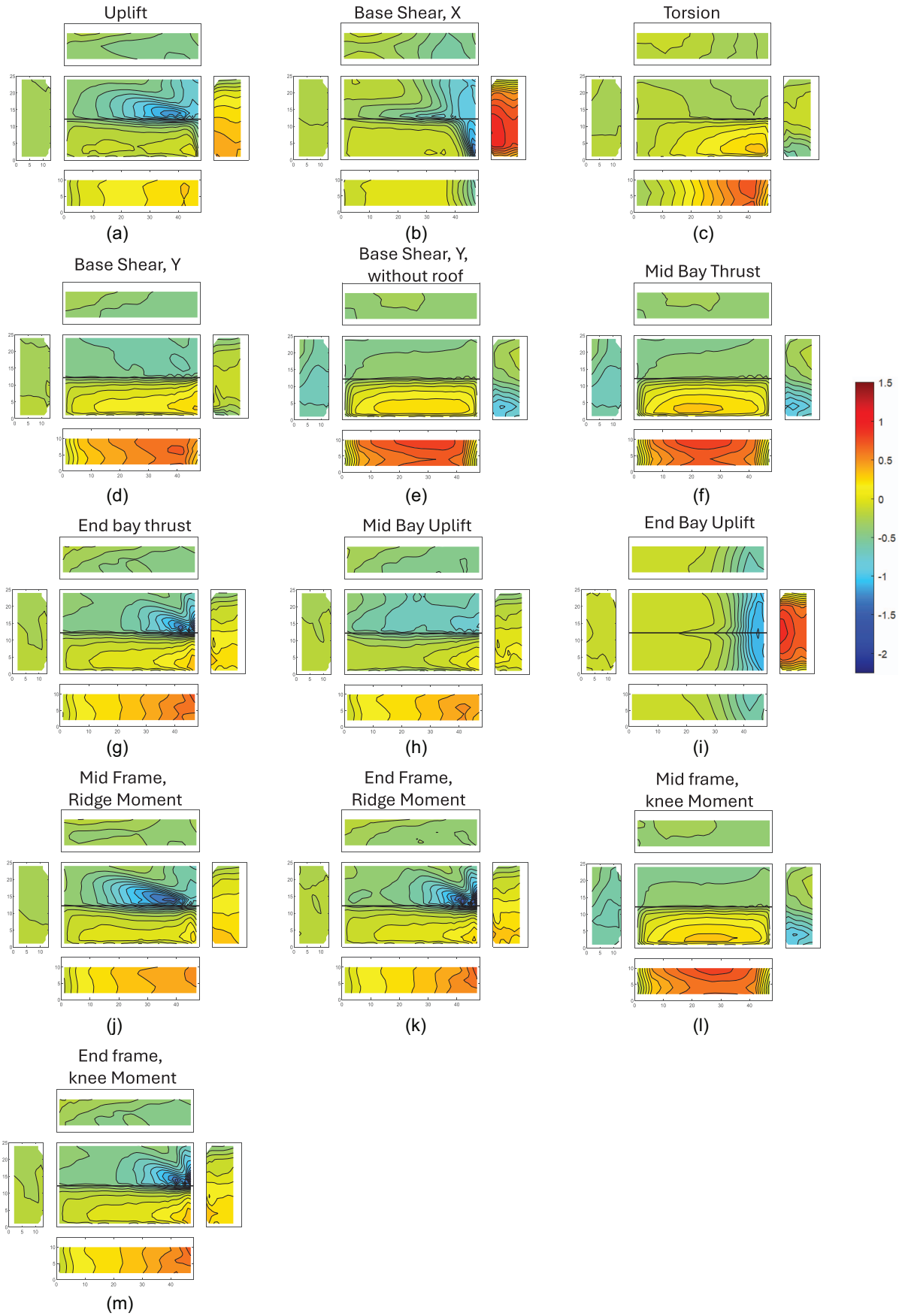

Fig. 15. (Color) Typical Cp_{LRC} distribution associated with critical structural responses for low-rise buildings with 6:12 sloped gable roofs, $d \times w \times h = 48 \times 24.38 \times 12.19$ m.

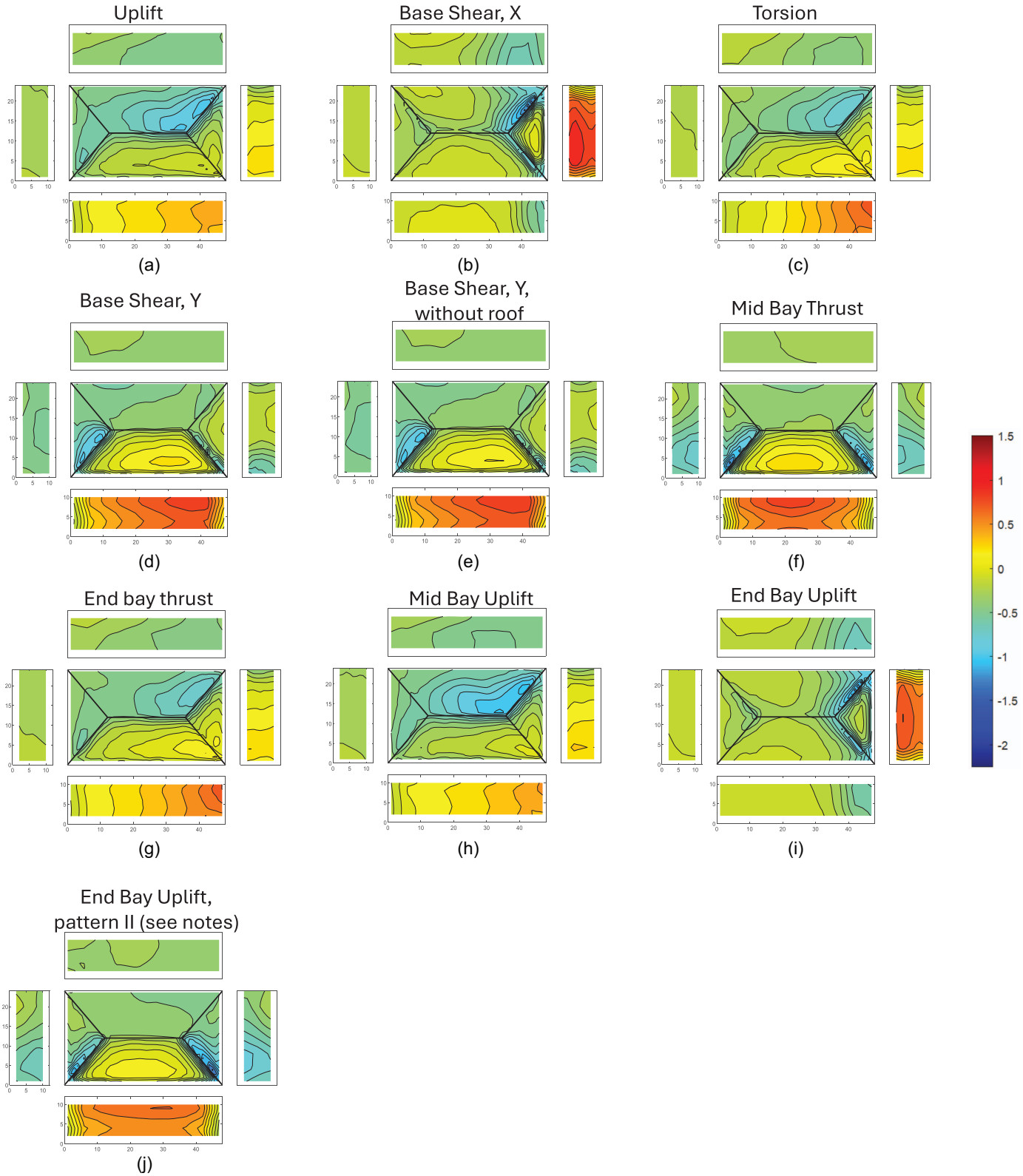

Fig. 16. (Color) Typical Cp_{LRC} distribution associated with critical structural responses for low-rise buildings, 6:12 sloped hip roofs, $d \times w \times h = 48 \times 24.38 \times 12.19$ m.

tunnel data from 85 building models were employed in this study, covering a wide range of geometry ratios, roof shapes, and roof slopes. For each building model, critical structural responses were identified. Peak values of these responses were obtained, and the equivalent pressure distributions associated with the peak responses were studied. Most responses fell into a few typical patterns. The zone shape and sizes for design load cases were determined based on these patterns to represent the realistic pressure distribution. The zone sizes and pressure coefficients are given as functions of nondimensional geometric parameters of the buildings. The results

J. Struct. Eng., 2025, 151(11): 04025182

show that this approach allows the provisions to better capture the variations caused by the building shape.

The final design load cases and pressure coefficients were determined using a procedure that included an optimization method for pressure coefficients that minimized the difference between the results and the source wind tunnel data. The final load cases generally were retained from the existing Chapter 27, and only one new subcase was introduced. Compared with the existing Chapter 27 and 28 provisions, the proposed provisions are a significant improvement in matching the wind tunnel data, for both the magnitude and the trends among different building shapes.

Appendix. Equivalent Peak Pressure Distributions (CP_{LRC}) Associated with Critical Structural Responses of Selected Building Models

Fig. 14 plots the equivalent peak pressure distributions (Cp_{LRC}) associated with critical structural responses for the low-rise building model with a 1:12 sloped roof, $d \times w \times h = 38.1 \times 24.4 \times 12.2$ m. Figs. 15 and 16 plot corresponding results for building models with 6:12 sloped gable and hip roofs, respectively, $d \times w \times h = 48 \times 24.4 \times 12.2$ m. For the end-bay uplift, the patterns in Figs. 16(i and j) have similar peak values, with a relative difference of less than 2%; therefore, they both are considered critical.

Data Availability Statement

Some or all data, models, or code that support the findings of this study are available from the corresponding author upon reasonable request.

Acknowledgments

This work was funded by the Structural Engineering Institute of the ASCE. The authors gratefully acknowledge the support of an Advisory Group made up of members of the ASCE 7 Wind Loads Subcommittee, in particular Don Scott, who chaired the Advisory Group, and Larry Griffis, Dr. Tim Reinhold, and Dr. Peter Vickery, who provided significant guidance. Yitian Guo gratefully acknowledges Dr. Yuchao Xia for providing technical help in structural analysis.

Author Contributions

Yitian Guo: Data curation; Formal analysis; Investigation; Methodology; Writing – original draft; Writing – review and editing. Jin Wang: Data curation; Formal analysis; Investigation; Methodology; Writing – review and editing. Timothy John Acosta: Data curation; Formal analysis; Investigation; Writing – review and editing. Stefano Brusco: Data curation; Formal analysis; Investigation; Writing – review and editing. Gregory A. Kopp: Conceptualization; Funding acquisition; Methodology; Project administration; Supervision; Writing – review and editing.

References

Acosta, T. J., S. Brusco, Y. Guo, J. Wang, and G. A. Kopp. 2024. *Consolidation of the ASCE 7 MWFRS provisions. Part 2. Wind tunnel experiments on buildings with 6:12 roof slopes*. London: Western Univ.

Akins, R. E., J. A. Peterka, and J. E. Cermak. 1977. "Mean force and moment coefficients for buildings in turbulent boundary layers." *J. Wind Eng. Ind. Aerodyn.* 2 (3): 195–209. https://doi.org/10.1016/0167-6105(77)90022-8.

ASCE. 2000. *Minimum design loads for buildings and other structures*. ASCE 7-98. Reston, VA: ASCE.

ASCE. 2022. *Minimum design loads and associated criteria for buildings and other structures*. ASCE/SEI 7-22. Reston, VA: ASCE.

Cook, N. J. 1990. *The designer's guide to wind loading of building structures: Part 2, static structures*. Building Research Establishment Rep. Oxford, UK: Butterworth-Heinemann.

Cook, N. J., and J. R. Mayne. 1979. "A novel working approach to the assessment of wind loads for equivalent static design." *J. Wind Eng. Ind. Aerodyn.* 4 (2): 149–164. https://doi.org/10.1016/0167-6105(79)90043-6.

Davenport, A. G. 1967. "Gust loading factors." *J. Struct. Div.* 93 (3): 11–34. https://doi.org/10.1061/JSDEAG.0001692.

Davenport, A. G. 1977. *Wind loads on low-rise buildings: Final report of phases I and II*. Engineering Science Rep. BLWT-SS8. London: Western Univ.

Gumbel, E. J. 1958. *Statistics of extremes*. New York: Columbia University Press.

Guo, Y., G. A. Kopp, J. Wang, T. J. Acosta, and S. Brusco. 2024. *Consolidation of the ASCE 7 MWFRS provisions. Part 1. Methodology for obtaining the new aerodynamic coefficients and load cases*. London: Western Univ.

Ho, T. C. E., A. G. Davenport, and D. Surry. 1995. "Characteristic pressure distribution shapes and load repetitions for the wind loading of low building roof panels." *J. Wind Eng. Ind. Aerodyn.* 57 (2–3): 261–279. https://doi.org/10.1016/0167-6105(94)00106-N.

Ho, T. C. E., D. Surry, D. Morrish, and G. A. Kopp. 2005. "The UWO contribution to the NIST aerodynamic database for wind loads on low buildings: Part 1. Archiving format and basic aerodynamic data." *J. Wind Eng. Ind. Aerodyn.* 93 (1): 1–30. https://doi.org/10.1016/j.jweia.2004.07.006.

Holmes, J. D. 1997. "Equivalent time averaging in wind engineering." *J. Wind Eng. Ind. Aerodyn.* 72 (Nov): 411–419. https://doi.org/10.1016/S0167-6105(97)00266-3.

Kasperski, M., and H. J. Niemann. 1992. "The L.R.C. (load-response-correlation)-method a general method of estimating unfavourable wind load distributions for linear and non-linear structural behavior." *J. Wind Eng. Ind. Aerodyn.* 43 (1–3): 1753–1763. https://doi.org/10.1016/0167-6105(92)90588-2.

Kopp, G. A., J. Wang, Y. Guo, S. Brusco, and T. J. Acosta. 2025. "Assessment of the main wind force resisting system provisions of ASCE/SEI 7-22 for rigid buildings." *J. Struct. Eng.*

Kwon, D. K., and A. Kareem. 2014. "Revisiting gust averaging time and gust effect factor in ASCE 7." *J. Struct. Eng.* 140 (11): 06014004. https://doi.org/10.1061/(ASCE)ST.1943-541X.0001102.

Lawson, T. V. 1980. *Wind effects on buildings, Vol. 1 design applications*. London: Applied Science.

Lieblein, J. 1974. *Note on simplified estimators for Type I extreme-value distribution*. Rep. No. 75, 637. Gaithersburg, MD: NIST.

Nywening, M. 2006. *The effects of geometry on wind loads of low-rise buildings*. London: Univ. of Western Ontario.

Solari, G. 1993a. "Gust buffeting. I: Peak wind velocity and equivalent pressure." *J. Struct. Eng.* 119 (2): 365–382. https://doi.org/10.1061/(ASCE)0733-9445(1993)119:2(365).

Solari, G. 1993b. "Gust buffeting. II: Dynamic alongwind response." *J. Struct. Eng.* 119 (2): 383–398. https://doi.org/10.1061/(ASCE)0733-9445(1993)119:2(383).

Solari, G., and A. Kareem. 1998. "On the formulation of ASCE7-95 gust effect factor." *J. Wind Eng. Ind. Aerodyn.* 77 (Sep): 673–684. https://doi.org/10.1016/S0167-6105(98)00182-2.

Stathopoulos, T. G. 1979. *Turbulent wind action on low rise buildings*. London: Univ. of Western Ontario.

St. Pierre, L. M. S., G. A. Kopp, D. Surry, and T. C. E. Ho. 2005. "The UWO contribution to the NIST aerodynamic database for wind loads on low buildings: Part 2. Comparison of data with wind load provisions." *J. Wind Eng. Ind. Aerodyn.* 93 (1): 31–59. https://doi.org/10.1016/j.jweia.2004.07.007.

Wang, J., and G. A. Kopp. 2021a. "Comparisons of aerodynamic data with the main wind force–resisting system provisions of ASCE 7-16. I: Low-rise buildings." *J. Struct. Eng.* 147 (3): 04020347. https://doi.org/10.1061/(ASCE)ST.1943-541X.0002925.

Wang, J., and G. A. Kopp. 2021b. "Comparisons of aerodynamic data with the main wind force–resisting system provisions of ASCE 7-16. II: Mid- and high-rise buildings." *J. Struct. Eng.* 147 (3): 04020348. https://doi.org/10.1061/(ASCE)ST.1943-541X.0002922.

Wang, J., and G. A. Kopp. 2021c. "Gust effect factors for windward walls of rigid buildings with various aspect ratios." *J. Wind Eng. Ind. Aerodyn.* 212 (May): 104603. https://doi.org/10.1016/j.jweia.2021.104603.